Engineering Fracture Mechanics 77 (2010) 1153–1174

Contents lists available at ScienceDirect

Engineering Fracture Mechanics

journal homepage: www.elsevier.com/locate/engfracmech

On the constitutive relation of materials with microstructure using a potential-based cohesive model for interface interaction

Duc Ngo [a], Kyoungsoo Park [b], Glaucio H. Paulino [a,b,*], Yonggang Huang [c,d]

[a] Department of Mechanical Science and Engineering, University of Illinois at Urbana-Champaign, Urbana, IL 61801, United States
[b] Department of Civil and Environmental Engineering, University of Illinois at Urbana-Champaign, Urbana, IL 61801, United States
[c] Department of Civil and Environmental Engineering, Northwestern University, IL 60208, United States
[d] Department of Mechanical Engineering, Northwestern University, IL 60208, United States

ARTICLE INFO

Article history:
Received 29 June 2009
Received in revised form 10 January 2010
Accepted 12 January 2010
Available online 29 January 2010

Keywords:
PPR model
Micromechanics (Mori–Tanaka method)
Cohesive zone model
Particle/matrix debonding
Upscaling

ABSTRACT

Macroscopic constitutive relationship is estimated by considering the microscopic particle/matrix interfacial debonding. For the interfacial debonding, the PPR potential-based cohesive model is utilized. The extended Mori–Tanaka model is employed for micromechanics, while a finite element-based cohesive zone model is used for the computational model. Both models (theoretical and computational) agree well each other in representing the macroscopic constitutive relationship on the basis of the PPR model. The microscopic interfacial cohesive parameters of the PPR model are estimated from macroscopic composite material behavior. In addition, different microscopic debonding processes are observed with respect to different macroscopic constitutive relationships (e.g. hardening, softening, and snap-back).

1. Introduction

The connections between different length scales, for example macroscopic behavior and microscopic behavior, are essential in understanding physical material behavior. Micromechanics models have been utilized to estimate the effective macroscopic elastic response of composite materials [1,2]. For instance, the self-consistent method [3,4] approximates the effective elastic properties by embedding a particle in the infinite medium of unknown effective properties. The generalization of this method, called the generalized self-consistent method [5], consists of introducing the matrix layer with the prescribed volume fraction between a particle and the effective infinite medium. The Mori–Tanaka method [6] is developed to calculate the average internal stress in the matrix of a material containing inclusions with transformation strain. The extension of the Mori–Tanaka model describes constitutive behavior of composites with interface debonding [7].

Several researchers have linked microscopic matrix/particle behavior with macroscopic continuum and fracture including either non-cohesive or cohesive behavior. Yin et al. [8] developed a micromechanics-based elastic constitutive model for functionally graded materials (FGMs) with particle interactions. The model was extended to represent effective thermo-elastic behavior of FGMs [9]. Paulino et al. [10] developed a micromechanical damage model for two-phase FGMs, which considers the interfacial debonding of particles and pair-wise interactions between particles. Levy [11] theoretically investigated separation of the matrix/particle interface under biaxial load. Siegmund and Brocks [12] employed the modified Gurson relationship [13] to consider void nucleation and growth, and to calibrate fracture parameters of the exponential

* Corresponding author. Tel.: +1 217 333 3817; fax: +1 217 265 8041.
E-mail addresses: ducngo2@illinois.edu (D. Ngo), kpark16@illinois.edu (K. Park), paulino@illinois.edu (G.H. Paulino), y-huang@northwestern.edu (Y. Huang).

0013-7944/$ - see front matter © 2010 Elsevier Ltd. All rights reserved.
doi:10.1016/j.engfracmech.2010.01.007

Nomenclature

a	radius of a particle
a_1, a_2	radii of the large and small particles
b	size of the representative volume element
E	elastic modulus
E^m	elastic modulus of the matrix
E^p	elastic modulus of particles
$\bar{K}$	initial bulk modulus
K^m	elastic bulk modulus of the matrix
K^p	elastic bulk modulus of the particle
f	volume fraction of the representative volume element
f_1, f_2	volume fractions of the large and small particles
f_k	volume fraction of the kth particle
$\mathbf{I}$	second-order identity tensor
m, n	non-dimensional exponents in the PPR model
$\mathbf{M}^m$	elastic compliance tensor of matrix materials
$\mathbf{M}_k^p$	elastic compliance tensor of particle materials
$\mathbf{n}$	unit normal vector on the interface pointing into the matrix
N	number of particles in the matrix
S_k^{int}	debonding surface between particles of kth size and matrix
$[\mathbf{u}]_k$	displacement separation at the kth particle/matrix interface
$[u_n]$	average displacement discontinuity in the normal direction
$\mathbf{u}^m$	displacement on the interface of the matrix
$\mathbf{u}_k^p$	displacement on the interface of the kth particle
α, β	shape parameter indices in the PPR model
δ_n, δ_t	normal and tangential final crack opening widths
$\mathbf{\Delta}_k$	displacement separation at the kth particle/matrix interface
Δ_n, Δ_t	normal and tangential separations
$\bar{\boldsymbol{\varepsilon}}, \bar{\varepsilon}$	averaged strain in the representative volume element (or macroscopic stress)
$\boldsymbol{\varepsilon}^m$	microscopic strain in the matrix
$\bar{\boldsymbol{\varepsilon}}^m$	average strain in the matrix
$\boldsymbol{\varepsilon}_k^p$	microscopic strain in the kth particle
$\bar{\boldsymbol{\varepsilon}}_k^p$	average strain in the kth particle
$\bar{\boldsymbol{\varepsilon}}_k^{\text{int}}$	average strain due to the debonding between the kth particle and matrix
ϕ_n, ϕ_t	mode I and mode II fracture energies
Γ_n, Γ_t	energy constants in the PPR model
λ_n, λ_t	initial slope indicators in the PPR model
ν	Poisson's ratio
ν^m	Poisson's ratio of the matrix
ν^p	Poisson's ratio of particles
$\bar{\boldsymbol{\sigma}}, \bar{\sigma}$	averaged stress in the representative volume element (or macroscopic stress)
σ^{int}, T_n	normal cohesive stress at the particle/matrix interface
$\sigma_1^{\text{int}}, \sigma_2^{\text{int}}$	microscopic cohesive stresses of the large and small particles
$\sigma_{\max}$	normal cohesive strength
$\bar{\sigma}_{\max}$	macroscopic cohesive strength
$\boldsymbol{\sigma}^m$	microscopic stress in the matrix
$\bar{\boldsymbol{\sigma}}^m, \bar{\sigma}^m$	average stress in the matrix
$\boldsymbol{\sigma}_k^p$	microscopic stress in the kth particle
$\bar{\boldsymbol{\sigma}}_k^p, \bar{\sigma}^p$	average stress in the kth particle
τ^{int}, T_t	tangential cohesive stress at the particle/matrix interface
$\tau_{\max}$	tangential cohesive strength
Ω	volume of a composite material
Ω^m	volume of the matrix
Ω_k^p	volume of the kth particle

traction–separation relationship. Allen and Searcy [14] idealized the representative volume element (RVE) as fibrils that are surrounded by air, and obtained homogenized traction–separation relationships. Tan et al. [15] utilized digital image correlation technique to obtain macroscopic cohesive parameters. Based on these cohesive parameters, the extended Mori–Tanaka method was applied to obtain a microscale cohesive relationship for particle/matrix interface.

Micromechanical particle/matrix behaviors can be investigated by means of computational methods. Shen et al. [16,17] studied the effect of particle shape and distribution on the effective elastic and plastic responses under perfect bonding between matrix and particle within the finite element analysis framework. Cohesive elements were incorporated with the finite element analysis to represent the matrix/particle debonding process. Xu and Needleman [18] investigated void nucleation along the interface in conjunction with an interfacial cohesive relationship, and Finot et al. [19] demonstrated the influence of crack size, in addition to shape, spatial distribution, and volume fraction of the particles. Mogilevskaya and Crouch [20] employed the Galerkin boundary integral method to study an infinite elastic plane containing randomly distributed circular elastic inclusions with homogeneously imperfect interfaces. Carpinteri et al. [21] investigated snap-back instability in micro-structured composites under uniaxial displacement boundary conditions in conjunction with a contact formulation which handles cohesive forces.

Cohesive elements represent the nonlinear fracture process zone. The concept of the cohesive zone model can be found in the papers by Dugdale [22] and Barenblatt [23]. This concept has been widely utilized to characterize both microscopic and macroscopic fracture behavior. For example, Boone et al. [24] utilized nonlinear joint elements to simulate fracture process of rock, and Ingraffea et al. [25] considered bond-slip in reinforced concrete in conjunction with tension softening elements. Xu and Needleman [26] utilized a cohesive surface network to simulate fast crack growth in brittle solids. Han et al. [27] simulated delamination propagation between a face sheet and a core in a honeycomb composite panel, while Song et al. [28] studied fracture of viscoelastic materials (e.g. asphalt concrete) by using a bilinear cohesive zone model. Furthermore, Zhang et al. [29] investigated dynamic fracture and microbranching instability in brittle materials.

The constitutive relationship of the cohesive interface, i.e. the conjugate traction–separation relationship, can be obtained through potential-based models. For instance, Tvergaard and Hutchinson [30] introduced a one-dimensional potential, and Xu and Needleman [26] presented the popular exponential-based potential model. Recently, a unified potential-based cohesive model [31], called the PPR (Park–Paulino–Roesler) model, was proposed, which provides consistent constitutive relationships for both proportional and non-proportional separation paths.

In this paper, the constitutive relationship of materials with microstructure is investigated by using the potential-based PPR cohesive model for the interface relationship. This investigation is integrated with a theoretical micromechanics model and a finite element-based cohesive zone model. In addition, the fracture parameters of the PPR model are estimated in conjunction with a micromechanics model.

The paper is organized as follows. Section 2 presents a theoretical micromechanics model that accounts for particle/matrix interface debonding. Next, the potential-based constitutive model for the interface between particle and matrix is explained in Section 3. Afterwards, Section 4 investigates the influence of cohesive fracture parameters, particle size and volume fraction on the constitutive relation under hydrostatic tension loading. Section 5 integrates the theoretical model with the computational model through investigation of particle/matrix debonding under equi-biaxial tension loading. The cohesive parameters of the PPR model are determined using macroscopic cohesive behavior in Section 6. Finally, the key findings of the paper are summarized in Section 7.

2. Constitutive behavior of composites accounting for particle/matrix interface debonding

We consider a RVE with volume Ω of the composite material of N different particle sizes embedded in the matrix. We assume the particles and matrix materials as linearly elastic. We denote the matrix volume and particle volume of the kth particle size as Ω^m and Ω^p_k, respectively ($k = 1, \ldots, N$). The particle volume fraction f_k of the kth particle size is given by Ω^p_k/Ω. The average stresses in the matrix $\bar{\boldsymbol{\sigma}}^m$ and in the kth particle $\bar{\boldsymbol{\sigma}}^p_k$ are defined as $\bar{\boldsymbol{\sigma}}^m = \frac{1}{\Omega^m}\int_{\Omega^m} \boldsymbol{\sigma}^m\, dV$ and $\bar{\boldsymbol{\sigma}}^p_k = \frac{1}{\Omega^p_k}\int_{\Omega^p_k} \boldsymbol{\sigma}^p_k\, dV$, respectively, where $\boldsymbol{\sigma}^m$ is microscopic stress in the matrix, and $\boldsymbol{\sigma}^p_k$ is microscopic stress in the kth particle. The average stress in the RVE or macroscopic stress $\bar{\boldsymbol{\sigma}}$ is given in terms of $\bar{\boldsymbol{\sigma}}^m$ and $\bar{\boldsymbol{\sigma}}^p_k$ [32–35] by $\bar{\boldsymbol{\sigma}} = (1-f)\bar{\boldsymbol{\sigma}}^m + \sum_{k=1}^N f_k \bar{\boldsymbol{\sigma}}^p_k$, where $f = \sum_{k=1}^N f_k$.

The average strains in the matrix $\bar{\boldsymbol{\varepsilon}}^m$ and in the particles $\bar{\boldsymbol{\varepsilon}}^p_k$ are defined as $\bar{\boldsymbol{\varepsilon}}^m = \frac{1}{\Omega^m}\int_{\Omega^m} \boldsymbol{\varepsilon}^m\, dV$ and $\bar{\boldsymbol{\varepsilon}}^p_k = \frac{1}{\Omega^p_k}\int_{\Omega^p_k} \boldsymbol{\varepsilon}^p_k\, dV$, respectively, where $\boldsymbol{\varepsilon}^m$ is microscopic strain in the matrix, and $\boldsymbol{\varepsilon}^p_k$ is microscopic strain in the kth particle. The average strain in the RVE or macroscopic strain $\bar{\boldsymbol{\varepsilon}}$ is given in terms of $\bar{\boldsymbol{\varepsilon}}^m$ and $\bar{\boldsymbol{\varepsilon}}^p_k$ by [36]

$$\bar{\boldsymbol{\varepsilon}} = (1-f)\bar{\boldsymbol{\varepsilon}}^m + \sum_{k=1}^{N} f_k(\bar{\boldsymbol{\varepsilon}}^p_k + \bar{\boldsymbol{\varepsilon}}^{\text{int}}_k), \tag{1}$$

where $\bar{\boldsymbol{\varepsilon}}^{\text{int}}_k$ is the average strain which is contributed from the debonding interface S^{int}_k between particles of kth size and matrix. In fact, $\bar{\boldsymbol{\varepsilon}}^{\text{int}}_k$ is related to the separation

$$\boldsymbol{\Delta}_k = [\mathbf{u}]_k = \mathbf{u}^m - \mathbf{u}^p_k, \tag{2}$$

at the kth particle/matrix interface by

$$\bar{\boldsymbol{\varepsilon}}^{\text{int}}_k = \frac{1}{2\Omega^p_k}\int_{S^{\text{int}}} (\boldsymbol{\Delta}_k \otimes \mathbf{n} + \mathbf{n} \otimes \boldsymbol{\Delta}_k)\, dA, \tag{3}$$

where $\mathbf{u}^m$ and $\mathbf{u}^p_k$ are the displacements on the interface of the matrix and the kth particle, respectively, and $\mathbf{n}$ is the unit normal vector on the interface pointing into the matrix (positive sign convention).

The average strains in the matrix and kth particle are related to the correspondent average stresses by $\bar{\boldsymbol{\varepsilon}}^m = \mathbf{M}^m : \bar{\boldsymbol{\sigma}}^m$ and $\bar{\boldsymbol{\varepsilon}}_k^p = \mathbf{M}_k^p : \bar{\boldsymbol{\sigma}}_k^p$, where $\mathbf{M}^m$ and $\mathbf{M}_k^p$ are the elastic compliance tensors of matrix and particle materials respectively. Then, the averaged strain in the RVE (1) is rewritten as

$$\bar{\boldsymbol{\varepsilon}} = \mathbf{M}^m : \bar{\boldsymbol{\sigma}} + \sum_{k=1}^{N} f_k \left[(\mathbf{M}_k^p - \mathbf{M}^m) : \bar{\boldsymbol{\sigma}}_k^p + \bar{\boldsymbol{\varepsilon}}_k^{\text{int}} \right]. \tag{4}$$

Expression (4) shows that, in order to obtain the constitutive relation of macroscopic strain and macroscopic stress, the average stresses in particles $\bar{\boldsymbol{\sigma}}_k^p$ and the average strains from interface debonding $\bar{\boldsymbol{\varepsilon}}_k^{\text{int}}$ need to be determined in terms of macroscopic stress $\bar{\boldsymbol{\sigma}}$ or macroscopic strain $\bar{\boldsymbol{\varepsilon}}$.

2.1. Hydrostatic tension stress state

In this section, for simplicity in evaluating $\bar{\boldsymbol{\sigma}}_k^p$ and $\bar{\boldsymbol{\varepsilon}}_k^{\text{int}}$, we follow the approach by Tan et al. [36] by considering a case of identical spherical particles embedded in an isotropic matrix subjected to hydrostatic tension stress state $\bar{\boldsymbol{\sigma}} = \bar{\sigma}\mathbf{I}$, where $\mathbf{I}$ is the second-order identity tensor. We assume that all the particles are isotropic, and have the same elastic modulus and radius a. From the tensorial equations of macroscopic stress and strain, we obtain

$$\bar{\sigma}_{ii} = (1-f)\bar{\sigma}_{ii}^m + f\bar{\sigma}_{ii}^p, \tag{5}$$

$$\bar{\varepsilon}_{ii} = \frac{(1-2\nu^m)}{E^m}\bar{\sigma}_{ii} + f\left\{ \left[\frac{(1-2\nu^p)}{E^p} - \frac{(1-2\nu^m)}{E^m} \right] \bar{\sigma}_{ii}^p + \bar{\varepsilon}_{ii}^{\text{int}} \right\}, \tag{6}$$

where (E^m, ν^m) and (E^p, ν^p) are the elastic moduli and Poisson's ratios of the matrix and particles, respectively. The macroscopic stress $\bar{\sigma}$, the average stress in the matrix $\bar{\sigma}^m$, and the average stress in the particles $\bar{\sigma}^p$ are defined as

$$\bar{\sigma} = \bar{\sigma}_{ii}/3, \quad \bar{\sigma}^m = \bar{\sigma}_{ii}^m/3, \quad \bar{\sigma}^p = \bar{\sigma}_{ii}^p/3. \tag{7}$$

Hence Eq. (5) can be rewritten as

$$\bar{\sigma} = (1-f)\bar{\sigma}^m + f\bar{\sigma}^p. \tag{8}$$

The average strain contributed from the interface debonding $\boldsymbol{\varepsilon}_{ii}^{\text{int}}$ is determined from Eq. (3) as

$$\bar{\varepsilon}_{ii}^{\text{int}} = \frac{1}{\Omega^p}\int_{S^{\text{int}}} \Delta_n dA = \frac{3\Delta_n}{a}, \tag{9}$$

where $\Delta_n = [u_n]$ is the average displacement discontinuity (or separation) along the normal direction (or radial direction in this case) on the interfaces between particles and matrix. Therefore, from Eq. (6), the macroscopic strain $\bar{\varepsilon}$ can be obtained as

$$\bar{\varepsilon} = \frac{\bar{\varepsilon}_{ii}}{3} = \frac{1-2\nu^m}{E^m}\bar{\sigma} + f\left\{ \left(\frac{1-2\nu^p}{E^p} - \frac{1-2\nu^m}{E^m} \right) \bar{\sigma}^p + \frac{\Delta_n}{a} \right\}. \tag{10}$$

2.2. Extended Mori–Tanaka method under hydrostatic tension

To determine the relation of $\bar{\sigma}^p$ and Δ_n in terms of the macroscopic stress $\bar{\sigma}$, following the approach by Tan et al. [36], we extend the Mori–Tanaka method [6], which is widely used for composite materials with high particle volume fraction. In the Mori–Tanaka method, the average stress $\bar{\sigma}^p$ in particles is related to the average stress $\bar{\sigma}^m$ in the matrix instead of the macroscopic stress $\bar{\sigma}$. Therefore, we consider a single spherical particle of radius a in an infinite matrix subject to the remote hydrostatic tensile stress state $\bar{\sigma}^m\mathbf{I}$, shown in Fig. 1a. The average particle stress $\bar{\sigma}^p$ is uniform and equal to the normal stress, σ^{int}, at the particle/matrix interface. Due to interface debonding, the normal displacement (or displacement in the radial direction) has a jump at the particle/matrix interface. At the outside boundary of the particle, the normal displacement is given as $\frac{1-2\nu^p}{E^p}a\sigma^{\text{int}}$, while at the inner boundary of the matrix, the normal displacement is given as $\frac{a}{2E^m}\left[3(1-\nu^m)\bar{\sigma}^m - (1+\nu^m)\sigma^{\text{int}}\right]$. The normal separation or the separation along the radial direction, at the particle/matrix interface can be obtained as

$$\Delta_n = [u_n] = \left[\frac{3(1-\nu^m)\bar{\sigma}^m - (1+\nu^m)\sigma^{\text{int}}}{2E^m} - \frac{1-2\nu^p}{E^p}\sigma^{\text{int}} \right] a. \tag{11}$$

The average stress in the matrix $\bar{\sigma}^m$ can be expressed in terms of Δ_n and σ^{int} as

$$\bar{\sigma}^m = \frac{2E^m}{3(1-\nu^m)}\left[\sigma^{\text{int}}\left(\frac{1-2\nu^p}{E^p} + \frac{1+\nu^m}{2E^m} \right) + \frac{\Delta_n}{a} \right]. \tag{12}$$

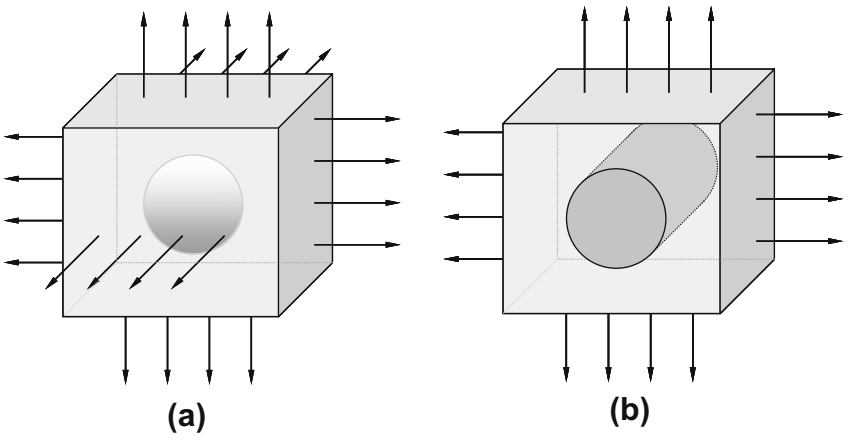

Fig. 1. (a) A spherical particle under hydrostatic tension stress state and (b) a cylindrical particle under equi-biaxial tension stress state.

Substituting Eq. (12) into the Eq. (8), we obtain the macroscopic stress $\bar{\sigma}$ in terms of Δ_n and σ^{int} as

$$\bar{\sigma} = (1-f)\frac{2E^m}{3(1-\nu^m)}\left[\sigma^{\text{int}}\left(\frac{1-2\nu^p}{E^p}+\frac{1+\nu^m}{2E^m}\right)+\frac{\Delta_n}{a}\right]+f\sigma^{\text{int}}. \tag{13}$$

The macroscopic strain $\bar{\varepsilon}$ in this case can be written as

$$\bar{\varepsilon} = \frac{1-2\nu^m}{E^m}\bar{\sigma}+f\left[\left(\frac{1-2\nu^p}{E^p}-\frac{1-2\nu^m}{E^m}\right)\sigma^{\text{int}}+\frac{\Delta_n}{a}\right]. \tag{14}$$

In order to obtain the constitutive relation between the macroscopic stress $\bar{\sigma}$ and macroscopic strain $\bar{\varepsilon}$ from Eqs. (13) and (14), the relationship between the normal stress σ^{int} and the normal separation Δ_n at the particle/matrix interface is needed. In this paper, the PPR cohesive model [31] for particle/matrix interface debonding is employed to establish the relation between the normal stress and the normal separation at the interface.

2.3. Extended Mori–Tanaka method under equi-biaxial tension

For equi-biaxial tension loading ($\bar{\sigma}$) under plane strain condition, we consider the case that all particles are isotropic, and are cylindrical with radius a, as shown in Fig. 1b. Once again, the extended Mori–Tanaka method is employed, in which the macroscopic stress $\bar{\sigma}$ can be obtained from Eq. (8), and the macroscopic strain $\bar{\varepsilon}$ can be obtained as

$$\bar{\varepsilon} = \frac{(1+\nu^m)(1-2\nu^m)}{E^m}\bar{\sigma}+f\left\{\left[\frac{(1+\nu^p)(1-2\nu^p)}{E^p}-\frac{(1+\nu^m)(1-2\nu^m)}{E^m}\right]\bar{\sigma}^p+\frac{\Delta_n}{a}\right\}, \tag{15}$$

where the average stress in the particle $\bar{\sigma}^p$ is uniform and equal to the normal stress at the particle/matrix interface (σ^{int}), which is related to the normal separation Δ_n by the cohesive relation of the PPR model. Accordingly, the average stress in the matrix $\bar{\sigma}^m$ is given by

$$\bar{\sigma}^m = \frac{E^m}{2(1-\nu^m)(1+\nu^m)}\left\{\left[\frac{1+\nu^m}{E^m}+\frac{(1-2\nu^p)(1+\nu^p)}{E^p}\right]\sigma^{\text{int}}+\frac{\Delta_n}{a}\right\}. \tag{16}$$

Notice that Eqs. (8), (15), and (16) provide the constitutive relation between macroscopic stress and macroscopic strain of composite materials accounting for interface debonding under equi-biaxial loading with plane strain conditions.

3. PPR: potential-based cohesive model for interface debonding

Park et al. [31] proposed a cohesive zone model for mixed mode fracture that overcomes some limitations of previous potentials such as ill-defined fracture parameters, large artificial compliance, and infinite final crack opening width. This model is based on the potential Ψ which is expressed in terms of normal separation $\Delta_n = [u_n]$ and tangential separation $\Delta_t = [u_t]$ along the fracture surface as

$$\Psi(\Delta_n,\Delta_t) = \min(\phi_n,\phi_t)+\left[\Gamma_n\left(1-\frac{\Delta_n}{\delta_n}\right)^{\alpha}\left(\frac{m}{\alpha}+\frac{\Delta_n}{\delta_n}\right)^{m}+\langle\phi_n-\phi_t\rangle\right]\left[\Gamma_t\left(1-\frac{|\Delta_t|}{\delta_t}\right)^{\beta}\left(\frac{n}{\beta}+\frac{|\Delta_t|}{\delta_t}\right)^{n}+\langle\phi_t-\phi_n\rangle\right], \tag{17}$$

where (Γ_n, Γ_t) are energy constants, (m, n) are non-dimensional exponents, (α, β) are shape parameters, and (δ_n, δ_t) are characteristic length scales. In two-dimensions (2D), ϕ_n and ϕ_t are the mode I and mode II fracture energies, respectively. The energy constants (Γ_n, Γ_t) are related to the fracture energies by

$$\Gamma_n = (-\phi_n)^{\frac{\langle \phi_n - \phi_t \rangle}{\phi_n - \phi_t}} \left(\frac{\alpha}{m}\right)^m, \quad \Gamma_t = (-\phi_t)^{\frac{\langle \phi_t - \phi_n \rangle}{\phi_t - \phi_n}} \left(\frac{\beta}{n}\right)^n, \tag{18}$$

for the case of different fracture energies $(\phi_n \neq \phi_t)$, where $\langle . \rangle$ is the usual Macaulay bracket, i.e. $\langle x \rangle = \begin{cases} 0, (x < 0) \\ x, (x \geqslant 0) \end{cases}$. If the fracture energies are the same $(\phi_n = \phi_t)$, the energy constants are simplified as $\Gamma_n = -\phi_n \left(\frac{\alpha}{m}\right)^m, \Gamma_t = \left(\frac{\beta}{n}\right)^n$. The non-dimensional exponents (m, n) are evaluated by the shape parameter indices (α, β) and initial slope indicators (λ_n, λ_t) as follows (cf. [31]):

$$m = \frac{\alpha(\alpha - 1)\lambda_n^2}{(1 - \alpha\lambda_n^2)}, \quad n = \frac{\beta(\beta - 1)\lambda_t^2}{(1 - \beta\lambda_t^2)}. \tag{19}$$

The initial slope indicators (λ_n, λ_t) are defined as the ratios of the critical crack opening widths, where the corresponding cohesive stresses are maximum (tension and shear cohesive strengths), to the corresponding final crack opening widths. Hence, they control the elastic behavior in a cohesive relationship. Smaller values of these indicators give higher initial slope in the cohesive relation, and thus decrease artificial elastic deformation. The shape of the cohesive relation can be conveniently changed by using shape parameter indices. If (α, β) are larger than 2, the relationship has a convex softening shape. On the other hand, if (α, β) are smaller than 2, the relationship has a concave softening shape. For the case in which the two indices are equal to 2, the softening relation obtained is nearly linear.

Moreover, (δ_n, δ_t) are the normal and tangential final crack opening width, respectively,

$$\begin{aligned} \delta_n &= \frac{\phi_n}{\sigma_{\max}} \alpha\lambda_n (1 - \lambda_n)^{\alpha - 1} \left(\frac{\alpha}{m} + 1\right) \left(\frac{\alpha}{m}\lambda_n + 1\right)^{m-1} \\ \delta_t &= \frac{\phi_t}{\tau_{\max}} \beta\lambda_t (1 - \lambda_t)^{\beta - 1} \left(\frac{\beta}{n} + 1\right) \left(\frac{\beta}{n}\lambda_t + 1\right)^{n-1} \end{aligned} \tag{20}$$

with $(\sigma_{\max}, \tau_{\max})$ being the normal and shear cohesive strength, respectively.

The normal cohesive stress σ^{int} (or normal cohesive traction, T_n) and tangential cohesive stress τ^{int} (or tangential cohesive traction, T_t) at the interface can be obtained by taking the gradient of the potential as

$$\begin{aligned} \sigma^{\text{int}}(\Delta_n, \Delta_t) &= \frac{\Gamma_n}{\delta_n} \left[m \left(1 - \frac{\Delta_n}{\delta_n}\right)^{\alpha} \left(\frac{m}{\alpha} + \frac{\Delta_n}{\delta_n}\right)^{m-1} - \alpha \left(1 - \frac{\Delta_n}{\delta_n}\right)^{\alpha - 1} \left(\frac{m}{\alpha} + \frac{\Delta_n}{\delta_n}\right)^{m} \right] \\ &\quad \times \left[\Gamma_t \left(1 - \frac{|\Delta_t|}{\delta_t}\right)^{\beta} \left(\frac{n}{\beta} + \frac{|\Delta_t|}{\delta_t}\right)^{n} + \langle \phi_t - \phi_n \rangle \right] \\ \tau^{\text{int}}(\Delta_n, \Delta_t) &= \frac{\Gamma_t}{\delta_t} \left[n \left(1 - \frac{|\Delta_t|}{\delta_t}\right)^{\beta} \left(\frac{n}{\beta} + \frac{|\Delta_t|}{\delta_t}\right)^{n-1} - \beta \left(1 - \frac{|\Delta_t|}{\delta_t}\right)^{\beta - 1} \left(\frac{n}{\beta} + \frac{|\Delta_t|}{\delta_t}\right)^{n} \right] \\ &\quad \times \left[\Gamma_n \left(1 - \frac{\Delta_n}{\delta_n}\right)^{\alpha} \left(\frac{m}{\alpha} + \frac{\Delta_n}{\delta_n}\right)^{m} + \langle \phi_n - \phi_t \rangle \right] \frac{\Delta_t}{|\Delta_t|} \end{aligned} \tag{21}$$

to obtain the intrinsic cohesive constitutive model. When the normal separation Δ_n and tangential separation Δ_t reach their final crack opening widths (δ_n, δ_t), respectively, the normal cohesive stress σ^{int} and tangential cohesive stress τ^{int} vanish. If the separations are greater than their final crack opening widths, the corresponding cohesive stress is set to zero [31].

For tensile opening (mode I) fracture, McMeeking and Parks [37] showed that in modified compact tension tests, the stress state ahead of the crack tip is nearly hydrostatic. Tan et al. [15] also showed that, in 2D mode I fracture, the stress state is equi-biaxial within the cohesive zone ahead of the crack tip. For those special cases of loadings, the tangential cohesive stress vanishes and the normal cohesive stress in Eq. (21) can be simplified by taking the tangential separation $\Delta_t = 0$. Thus, we obtain the following intrinsic cohesive zone model for normal cohesive stress σ^{int} in terms of normal separation Δ_n as

$$\sigma^{\text{int}} = \frac{\phi_n}{\delta_n} \left(\frac{\alpha}{m}\right)^m \left(1 - \frac{\Delta_n}{\delta_n}\right)^{\alpha - 1} \left(\frac{m}{\alpha} + \frac{\Delta_n}{\delta_n}\right)^{m-1} (m + \alpha) \frac{\Delta_n}{\delta_n}. \tag{22}$$

This relation between the normal cohesive stress and the normal separation provides the cohesive relationship of the interface debonding along the normal direction and is illustrated in Fig. 2. For the sake of illustration, in this example, the tension cohesive strength $(\sigma_{\max})$ is chosen to be 10 MPa and the fracture energy for mode I (ϕ_n) is 1 N/m. The shape parameter index (α) is set to 3, while the initial slope indicator (λ_n) is selected as 0.005.

In the case of hydrostatic tension loading, the cohesive relation of σ^{int} in terms of Δ_n in Eq. (22) together with Eqs. (13) and (14), which represent the relation of macroscopic stress and strain in terms of σ^{int} and Δ_n, provides a system of

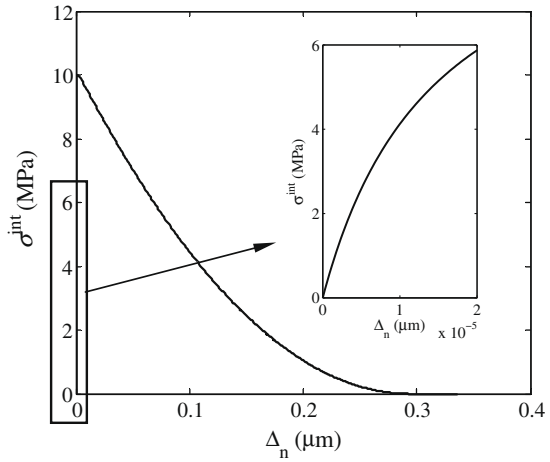

Fig. 2. Illustrative intrinsic cohesive relation of normal interface debonding.

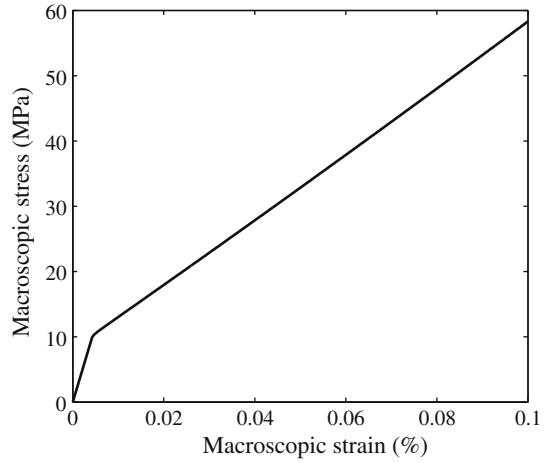

Fig. 3. Stress versus strain curve of the material (a = 100 μm).

parametric equations in terms of the normal displacement separation Δ_n. Based on these equations, we can determine the constitutive relation between the macroscopic stress and strain of composite materials.

4. Micromechanics investigation of the PPR Model

In the previous sections, we have shown that macroscopic constitutive behavior of composite materials accounting for particle/matrix debonding can be obtained by incorporating the PPR cohesive relation into the micromechanics model. In this section, we investigate the effect of relevant PPR cohesive parameters, e.g. particle size and volume fraction, on the macroscopic constitutive behavior of the material. For simplicity, we apply our micromechanics model in the hydrostatic tension loading case, presented in Section 2, to the limit when the material is homogenous. Hence, both matrix and particle have the same material properties. At this time, the particles have the role as microstructure in the material, and the volume fraction (f) represents the amount of interface between the microstructure and the material. We still assume that all the microstructures are isotropic and have the same spherical shape with the radius a (see Fig. 1a). Thus, the macroscopic stress and strain in Eqs. (13) and (14) are simplified to

$$\bar{\sigma} = (1-f)\frac{2E}{3(1-\nu)}\frac{\Delta_n}{a} + \sigma^{\text{int}}, \tag{23}$$

$$\bar{\varepsilon} = \frac{1}{3K}\bar{\sigma} + f\frac{\Delta_n}{a}, \tag{24}$$

where K is the elastic bulk modulus of the material and σ^{int} is described in terms of normal separation Δ_n as shown in Eq. (22).

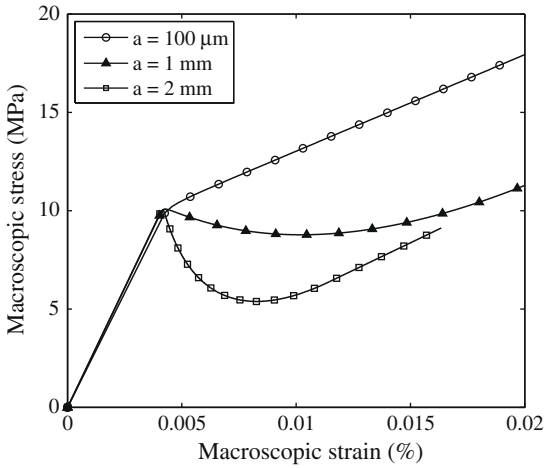

Fig. 4. Effect of particle size on the constitutive relation ($f = 0.6$).

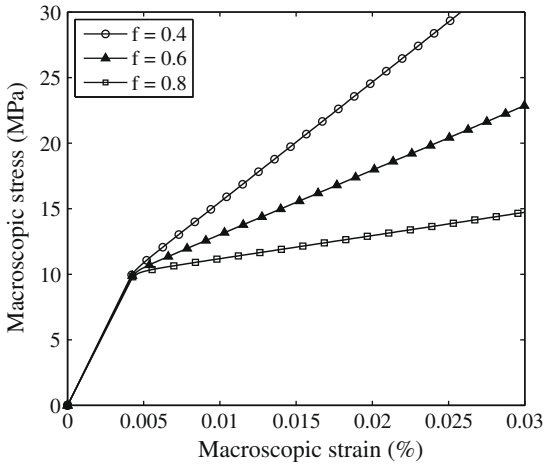

Fig. 5. Effect of particle volume fraction on the constitutive relation in the case of fine particles ($a = 100$ μm).

From the two parametric equations in terms of normal separation, i.e. Eqs. (23) and (24), the macroscopic constitutive relation of the material can be determined as illustrated in Fig. 3 for particle size $a = 100$ μm. In Fig. 3, the values of elastic modulus and Poisson's ratio for both matrix and particle are chosen as $E = 122$ GPa and $\nu = 0.25$, respectively. The PPR cohesive parameters are the same as the ones used in Fig. 2, where cohesive strength $\sigma_{\max} = 10$ MPa, fracture energy $\phi_n = 1$ N/m, shape parameter index $\alpha = 3$ and initial slope indicator $\lambda_n = 0.005$. Notice that the geometrical and material parameters, in this section and also in the next section, are illustrative quantities chosen to investigate the overall behavior of composites accounting for particle/matrix debonding with the PPR cohesive relation. The investigation of an actual material is provided later in this paper (Section 6).

4.1. Effect of particle size

We investigate the effect of particle size while fixing all other parameters. Fig. 4 illustrates the macroscopic stress–strain curves of the material for different particle sizes. The material tends to display hardening behavior when the size of the particles is small, while softening behavior appears in the case of large particles.

4.2. Effect of particle volume fraction

Similarly, to examine the effect of particle volume fraction on the macroscopic constitutive relation, we change the value of the particle volume fraction and fix all other parameters. In the case of fine particles ($a = 100$ μm), Fig. 5 illustrates how the macroscopic stress–strain relation is influenced by the particle volume fraction. A higher volume

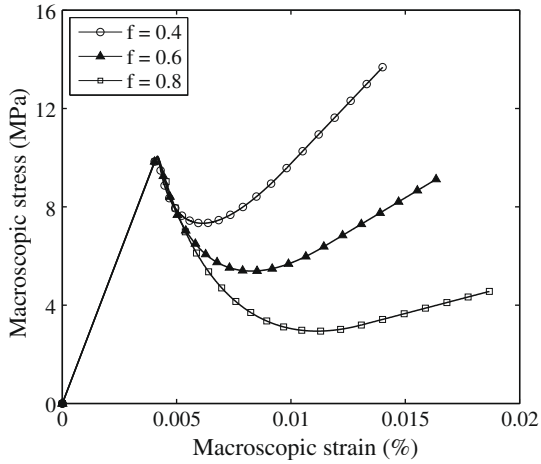

Fig. 6. Effect of particle volume fraction on the constitutive relation in the case of coarse particles (a = 2 mm).

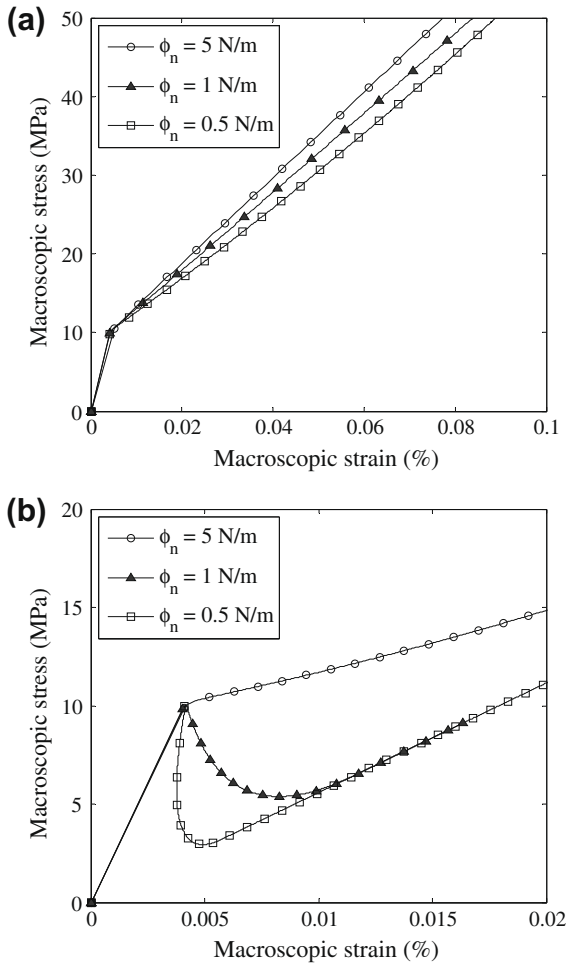

Fig. 7. Effect of cohesive energy on the constitutive relation with volume fraction f = 0.6: (a) a = 100 μm and (b) a = 2 mm.

fraction of particle gives a smaller slope in the hardening region of the stress–strain curve. For the case of coarse particles (a = 2 mm), Fig. 6 shows that the softening effect increases when the volume fraction increases.

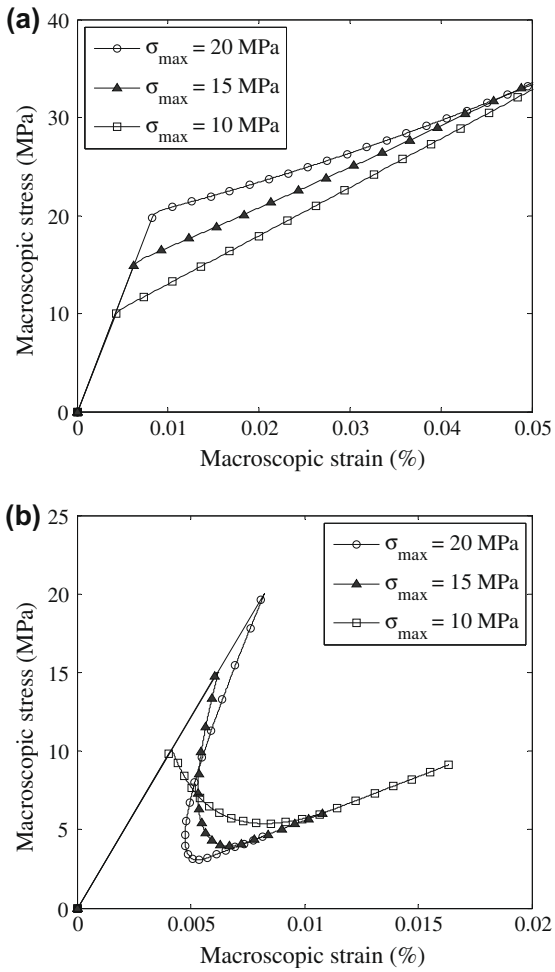

Fig. 8. Effect of cohesive strength on the constitutive relation with volume fraction $f = 0.6$: (a) $a = 100$ μm and (b) $a = 2$ mm.

4.3. Effect of cohesive energy

The influence of cohesive energy on the macroscopic constitutive relation is examined and shown in Fig. 7. When the cohesive energy increases, more energy is needed to separate the particle and the matrix, therefore, the stress–strain curve displays increased hardening effect.

4.4. Effect of cohesive strength

The increase of the cohesive strength of the interface debonding relation provides higher stress before the macroscopic constitutive relation reaches the hardening–softening region. However, because the cohesive energy is fixed, the higher cohesive strength gives a smaller final normal separation. Hence, the complete debonding occurs earlier, which is shown clearly in the case of a large particle in Fig. 8b.

4.5. Brittleness number

The brittleness number [21,38] reflects the effect of particle size, cohesive strength, and fracture energy. The brittleness number for the previous examples in Figs. 4–8 is calculated in Table 1, where it is defined as $\beta_K = a\sigma_{\max}^2/\phi_n E$ (free from scaling factors), which agrees with Hillerborg's definition [39]. In general, a high brittleness number leads to softening behavior, while a low brittleness number results in hardening behavior, as illustrated in Figs. 4–8. However, the brittleness number is unable to capture the effect of volume fraction within the same framework. Furthermore, one may misunderstand actual material behavior if one relies only on the brittleness number. For example, let us consider the following three cases:

Table 1
Investigation of brittleness number for the examples in Figs. 4–8.

Figure	f	a (mm)	σ_{max} (MPa)	ϕ_n (N/m)	E (GPa)	Brittleness number
4	0.6	0.1/1/2	10	1	122	0.082/0.820/1.639
5	0.4/0.6/0.8	0.1	10	1	122	0.082
6	0.4/0.6/0.8	2	10	1	122	1.639
7a	0.6	0.1	10	5/1/0.5	122	0.016/0.082/0.164
7b	0.6	2	10	5/1/0.5	122	0.328/1.639/3.279
8a	0.6	0.1	10/15/20	1	122	0.082/0.184/0.328
8b	0.6	2	10/15/20	1	122	1.639/3.689/6.557

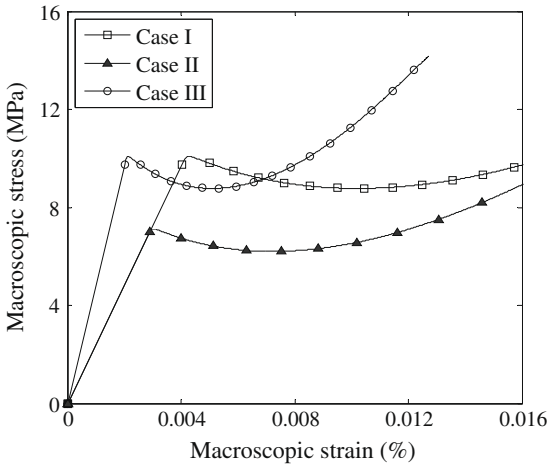

Fig. 9. Macroscopic stress versus strain relationships for $f = 0.6$ and the same brittleness number ($\beta_K = 0.82$).

- Case I: $a = 1$ mm, $\sigma_{max} = 10$ MPa, $\phi_n = 1$ N/m, $E = 122$ GPa.
- Case II: $a = 2$ mm, $\sigma_{max} = 7.07$ MPa, $\phi_n = 1$ N/m, $E = 122$ GPa.
- Case III: $a = 2$ mm, $\sigma_{max} = 10$ MPa, $\phi_n = 1$ N/m, $E = 244$ GPa.

all of which provide the same brittleness number, i.e. $\beta_K = 0.82$. The macroscopic stress versus strain relationships are plotted in Fig. 9 considering $f = 0.6$. Although the three cases lead to the same brittleness number, they result in different macroscopic stress versus strain relationships.

5. Theoretical and computational investigation of materials with microstructure accounting for particle/matrix interface debonding

Particle/matrix debonding process and macroscopic constitutive relationships of composite material are investigated by utilizing both micromechanics and finite element method by means of an integrated approach. The geometry of the unit cell for computational investigation is illustrated in Fig. 10a (cf. Fig. 1b). As indicated before, the particle sizes: (a) are 100 μm, 1 mm and 2 mm, while the size of the RVE (b) is calculated on the basis of the particle volume fraction of the microstructures. The elastic modulus of both matrix and particle is 122 GPa, the Poisson's ratio is 0.25, and the particle volume fraction is 0.6 for this study. In addition, in the computational simulation, the mode II fracture parameters $(\phi_t, \tau_{max}, \beta, \lambda_t)$ are assumed to be the same as the mode I fracture parameters $(\phi_n, \sigma_{max}, \alpha, \lambda_n)$ in the PPR model.

In the theoretical model, the extended Mori–Tanaka method under equi-biaxial loading with plane strain condition is employed. The expressions of the macroscopic strain (15), the average stress in the matrix (16), and the cohesive relationship of the PPR model (22) lead to the constitutive relationship between macroscopic stress and macroscopic strain, as discussed in Section 2.3.

In the computational simulation, a two-dimensional plane strain condition is employed, and a quarter of the unit cell is analyzed because of symmetry along the horizontal and vertical directions (see Fig. 10). Both the matrix and particle are represented by volumetric elements while the interface debonding between particle and matrix is characterized by cohesive surface elements using the PPR model [31]. Cohesive surface elements are implemented as a user-defined element subroutine in the commercial software ABAQUS. The finite element mesh is illustrated in Fig. 11a, and cohesive surface elements are inserted *a priori* along the particle/matrix interface, as indicated by a thick solid line. The number of bulk elements is 6826 (Q4), the number of cohesive elements is 200, and the total number of nodes is 7128. The size of cohesive elements is 16 μm

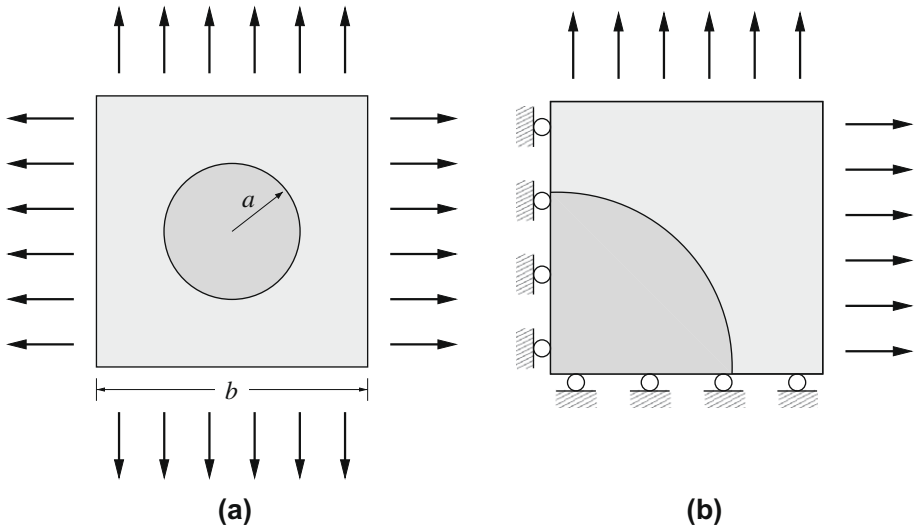

Fig. 10. (a) Geometry of the square unit cell (size b) with particle of radius a and (b) boundary conditions for the computational modeling.

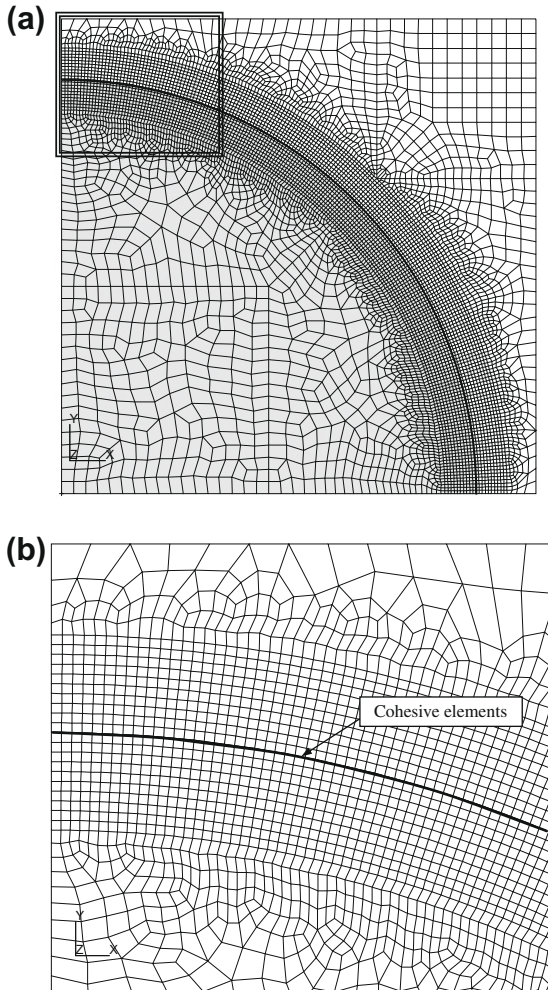

Fig. 11. (a) Finite element mesh of the unit cell and (b) zoom of the mesh along the interface between particle (a = 2 mm) and matrix.

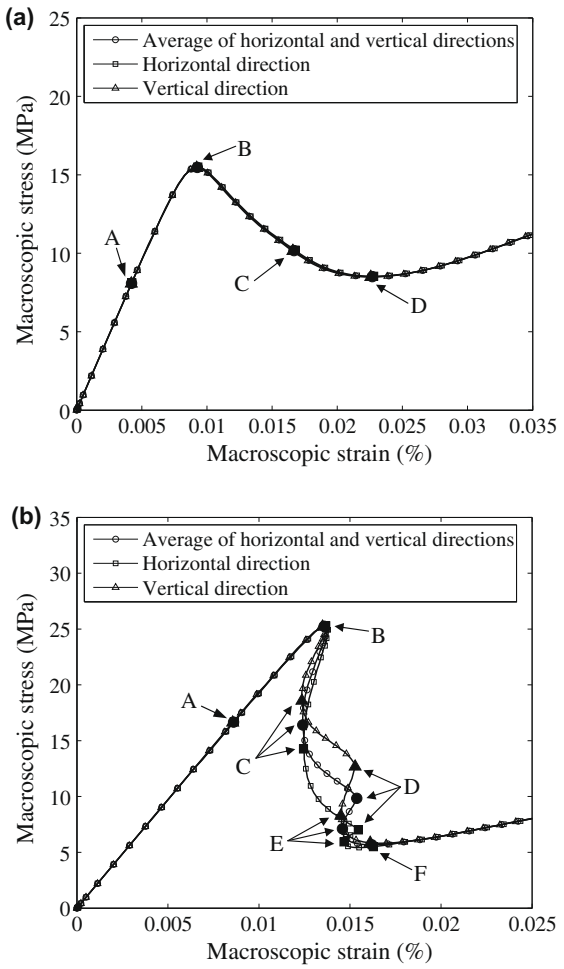

Fig. 12. Computational results displaying macroscopic strain versus strain along the horizontal and vertical directions with cohesive strength of: (a) 15 MPa and (b) 25 MPa.

for the particle size of 2 mm, which is small enough to capture the nonlinear particle/matrix debonding process. We obtained almost the same computational results using the cohesive element size of 32 μm as those with the size of 16 μm. A zoomed-in region of the mesh around the interface is shown in Fig. 11b, and the mesh in this region is uniform.

Displacement boundary conditions are applied to the unit cell. The left and bottom edges in the finite element mesh are fixed along the horizontal and vertical directions (Fig. 10b), respectively, due to the symmetry of the unit cell. Along the right and top edges, uniform displacement is applied. In order to improve convergence of computational simulation in the matrix/particle debonding process, especially for a case of snap-back instability, slightly higher displacement (e.g. 1%) is applied along the horizontal direction. The averaged macroscopic strain is evaluated by dividing the corresponding displacement along the edge by half of the RVE size ($b/2$), while the averaged macroscopic stress is calculated by dividing the summation of reaction forces along the edge by half of the RVE size ($b/2$).

In this section, the particle/matrix debonding process is observed for different types of macroscopic constitutive relationships. Next, the effect of microstructural size and material parameters on the macroscopic stress–strain relationship is theoretically and numerically investigated.

5.1. Particle/matrix debonding process

Different types of particle/matrix debonding processes are observed for different types of the macroscopic constitutive relationships resulting from the change of microstructural size or material properties. In this study, for the configuration (Fig. 10b) with the particle size $a = 2$ mm, the fracture energy and the shape parameter are fixed as $\phi_n = 5$ N/m and $\alpha = 3$. The initial slope indicator is selected as a small value (e.g. $\lambda_n \in [0.002, 0.01]$) within numerical stability limits. With the cohesive strengths of $\sigma_{\max} = 15$ MPa and 25 MPa, the averaged macroscopic stress–strain relationships along the horizontal and vertical directions are plotted in Fig. 12. When the cohesive strength is 15 MPa, the macroscopic stress–strain relationship

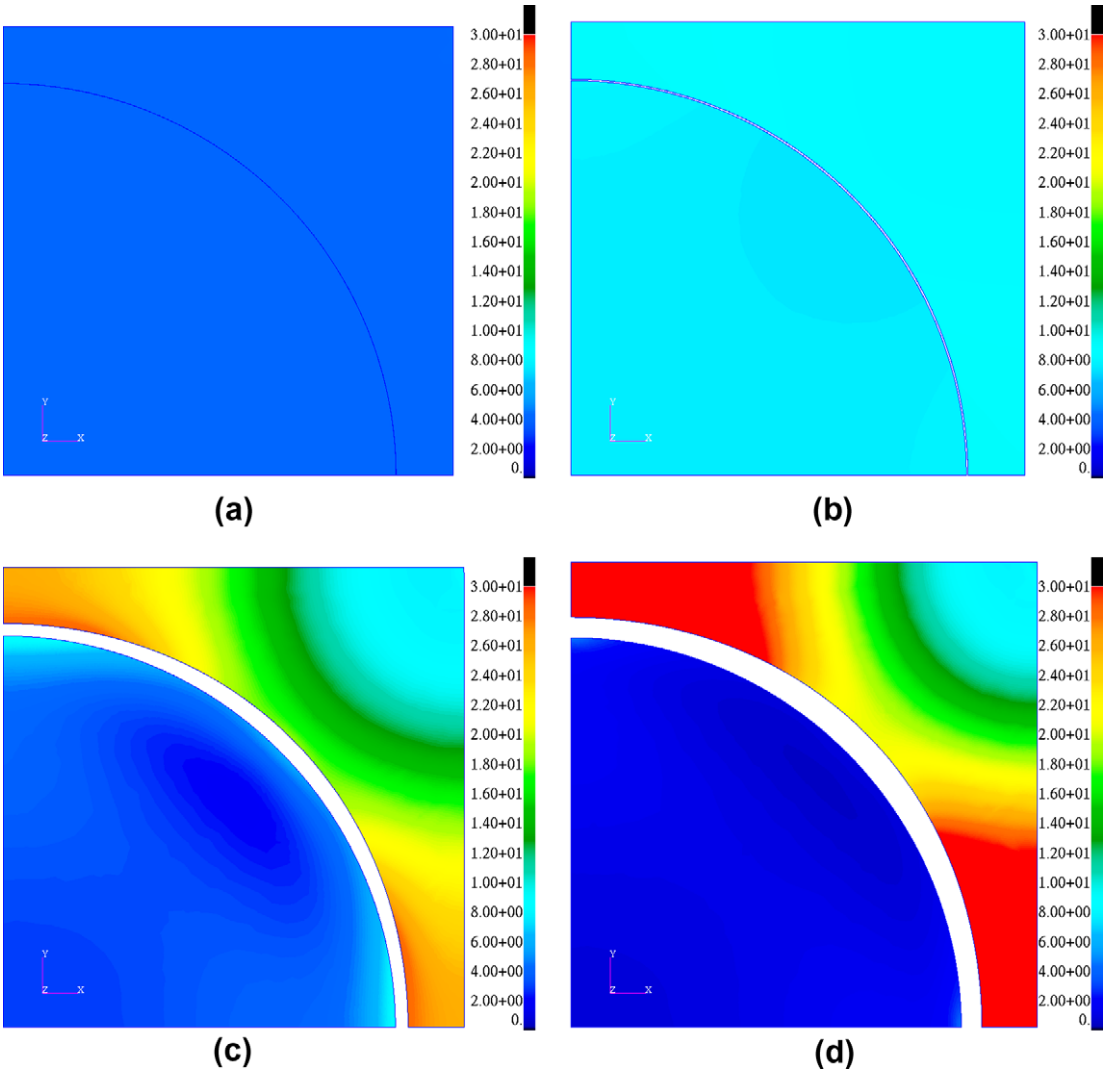

Fig. 13. Von Mises stress distribution for particle/matrix debonding process with softening behavior (Fig. 12a: σ_{max} = 15 MPa) at the stage of: (a) point A, (b) point B, (c) point C, and (d) point D.

displays softening behavior (Fig. 12a). On the other hand, if the cohesive strength is 25 MPa, the macroscopic stress–strain relationship demonstrates snap-back instability behavior, as shown in Fig. 12b.

For the case of softening behavior (Fig. 12a: σ_{max} = 15 MPa), the particle/matrix debonding process is observed at the four points: elastic range (point A), peak point (point B), softening range (point C), and complete separation (point D). Accordingly, Fig. 13 illustrates the deformed shape and von Mises stress distribution at each point. Before reaching the peak point (point B), the von Mises stress distribution is uniform, i.e. elastic stage (Fig. 13a). After the peak point (Fig. 13b), stress in the particle decreases while stress in matrix increases due to the particle/matrix debonding (Fig. 13c). In this softening stage (e.g. point C), the separation along the particle/matrix interface is uniform. Finally, the stress in the particle reaches zero, and the complete debonding occurs, as shown in Fig. 13d. In this case, the debonding process is stable, and thus the separation is uniform along the interface.

When the macroscopic stress–strain relationship exhibits snap-back instability (Fig. 12b: σ_{max} = 25 MPa), the particle/matrix debonding process is different from the previous case. Until the microstructure reaches the elastic limit (point B), the von Mises stress is generally uniform (Fig. 14a and b), and almost no debonding occurs. At the onset of the snap-back instability, particle and matrix start to debond from each other. Because of the snap-back instability, unstable debonding process is expected. Thus the separation along the particle/matrix interface may not be uniform. In this numerical investigation, for example, the debonding occurs along the horizontal direction first, which corresponds to the stage from point B (Fig. 14b) to point C (Fig. 14c). The initiated crack propagates along the interface between matrix and particle, which corresponds to the stage from point C (Fig. 14c) to point D (Fig. 14d). The crack propagation in this stage is stable in the sense that

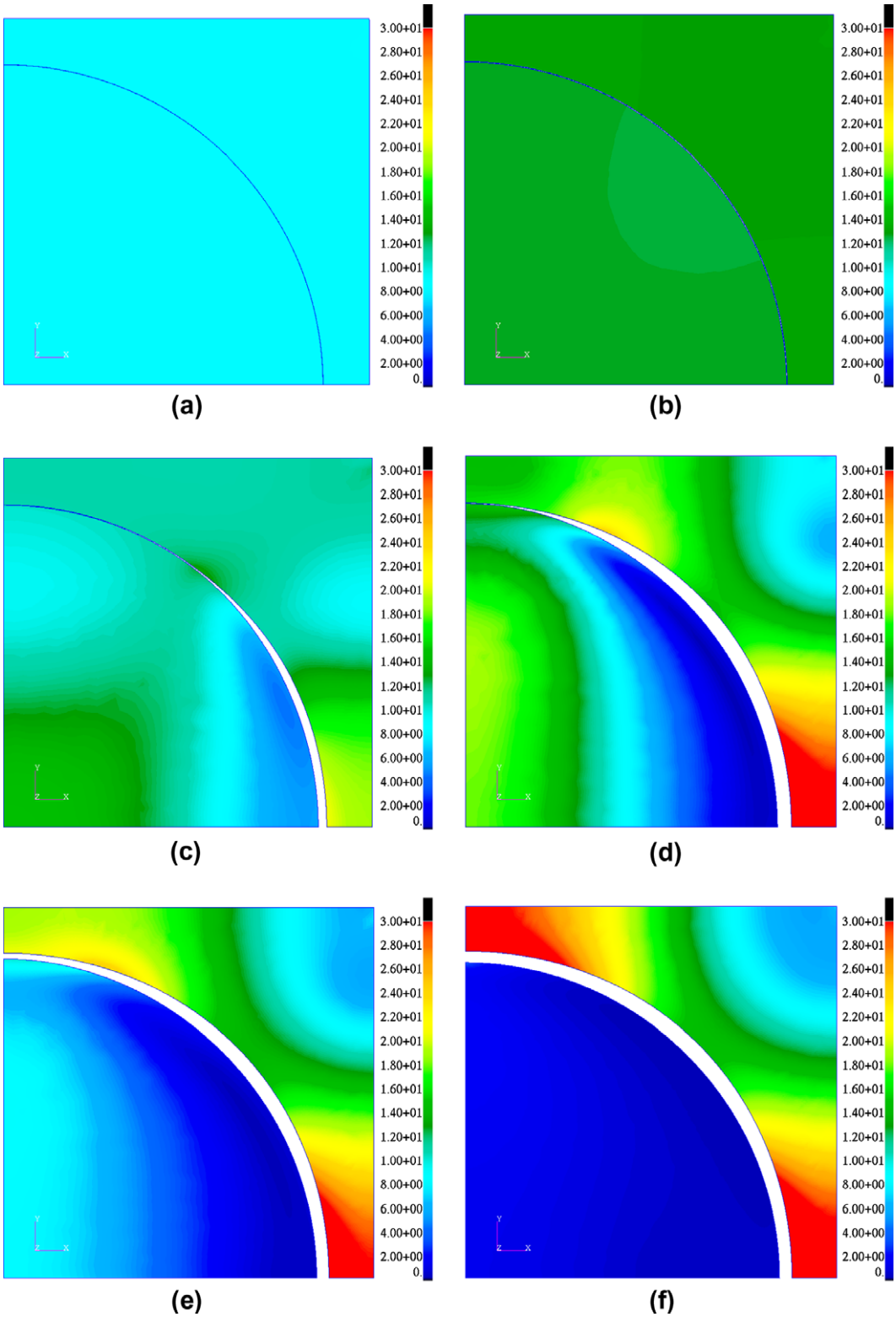

Fig. 14. Von Mises stress distribution for particle/matrix debonding process with snap-back behavior (Fig. 12b: σ_{max} = 25 MPa) at the stage of: (a) point A, (b) point B, (c) point C, (d) point D, (e) point E, and (f) point F.

the increase of separation along the interface leads to the decrease of the macroscopic stress, i.e. softening behavior. Next, a secondary snap-back instability is observed, which leads to the debonding along the vertical direction, i.e. the stage from

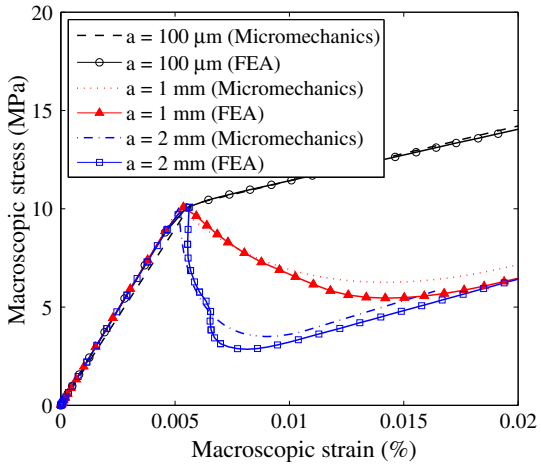

Fig. 15. Effect of the particle size on the constitutive relationship.

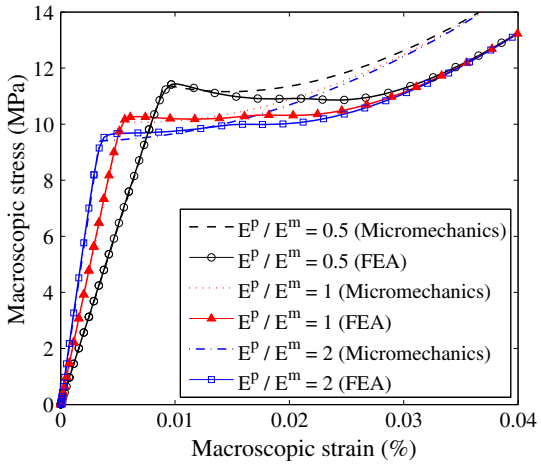

Fig. 16. Effect of the ratio of elastic modulus on the constitutive relationship.

point D to point E. In the end, the complete separation occurs at point F, as shown in Fig. 14f. The von Mises stress in the particle becomes zero, and stress concentration is observed in the matrix.

5.2. Effect of microstructure size

The macroscopic constitutive relationship varies with respect to the change of the microstructure size, elastic modulus, fracture energy and cohesive strength. First, the effect of microstructure size on macroscopic behavior is investigated. The particle sizes are 2 mm, 1 mm, and 100 μm; with particle volume fraction $f = 0.6$. The fracture energy is $\phi_n = 1$ N/m, the cohesive strength is $\sigma_{max} = 10$ MPa, and the shape parameter is $\alpha = 3$. For the given fracture parameters, the constitutive relationships for each particle size demonstrate similar elastic behavior (i.e. almost linear) until the macroscopic stress reaches 10 MPa, which corresponds to the adopted cohesive strength. After the elastic limit is reached, the fine particle ($a = 100$ μm) material demonstrates hardening behavior while the coarse particle ($a = 2$ mm) material displays softening behavior, as shown in Fig. 15.

5.3. Effect of particle elastic modulus

Next, the effect of the particle elastic modulus is studied. The elastic modulus of the matrix is fixed ($E^m = 122$ MPa), while the elastic modulus of particle (E^p) is selected as 61 MPa, 122 MPa, and 244 MPa, which leads to the ratio of the particle elastic modulus to the matrix elastic modulus of 0.5, 1, and 2, respectively. The selected size of particle is 2 mm with volume fraction $f = 0.6$. The fracture energy is $\phi_n = 5$ N/m with cohesive strength of $\sigma_{max} = 10$ MPa, and shape parameter $\alpha = 3$. The

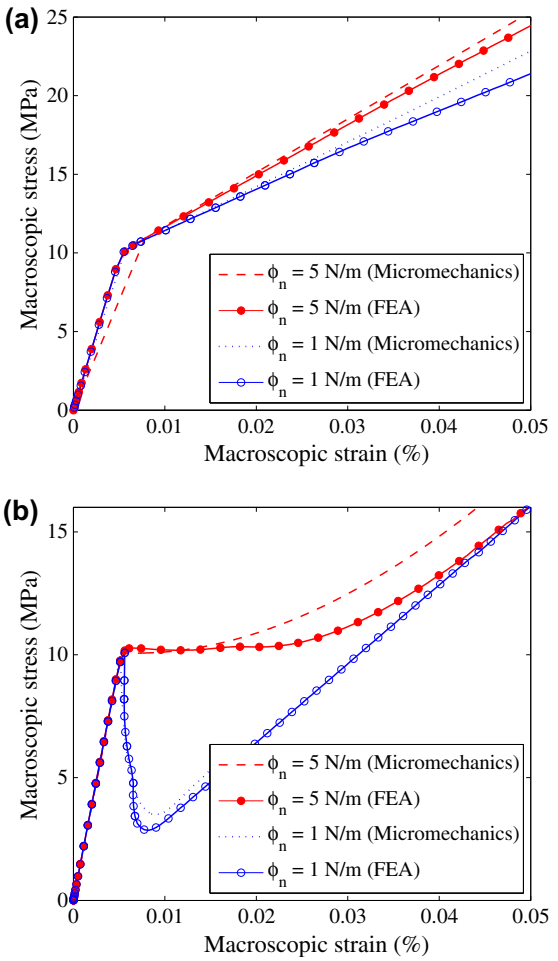

Fig. 17. Effect of the fracture energy on the constitutive relationship with particle size of: (a) 100 μm and (b) 2 mm.

higher elastic modulus of particles results in stiffer elastic behavior and shorter elastic range. The lower elastic modulus of particles leads to a slightly higher macroscopic stress at the elastic limit, as shown in Fig. 16. At larger macroscopic strain, complete debonding occurs, and thus the elastic modulus of particle does not influence the macroscopic stress–strain relationship.

5.4. Effect of fracture energy and particle size

The change of cohesive fracture parameters also leads to different macroscopic constitutive relationships. Two particle sizes (a = 2 mm and 100 μm) are investigated with respect to the fracture energies of ϕ_n = 1 N/m and 5 N/m. The cohesive strength is σ_{max} = 10 MPa, and the shape parameter is α = 3. For each particle size, elastic behavior is almost the same, as shown in Fig. 17. After the averaged macroscopic stress reaches the elastic limit, which almost corresponds to the cohesive strength (10 MPa), the larger fracture energy provides higher load capacity for both coarse and fine particle sizes. The increase of fracture energy changes the macroscopic stress–strain relationship from softening behavior to hardening behavior for the coarse particle (a = 2 mm).

5.5. Effect of cohesive strength and particle size

The effect of the cohesive strength is also investigated. The particle sizes are a = 2 mm and 100 μm; and the cohesive strengths are σ_{max} = 10 MPa, 15 MPa, and 25 MPa. The fracture energy and the shape parameters are fixed as ϕ_n = 5 N/m and α = 3, respectively. In this simulation, the fine particle configuration demonstrates hardening behavior, while the coarse particle illustrates various post-peak load behaviors such as hardening, softening and snap-back, with respect to the change of cohesive strength (Fig. 18). The higher cohesive strength leads to higher macroscopic stress of the elastic limit. At the larger macroscopic strain, complete separation occurs along the interface between particle and matrix, and thus the macroscopic constitutive relationships become the same for the different cohesive strengths.

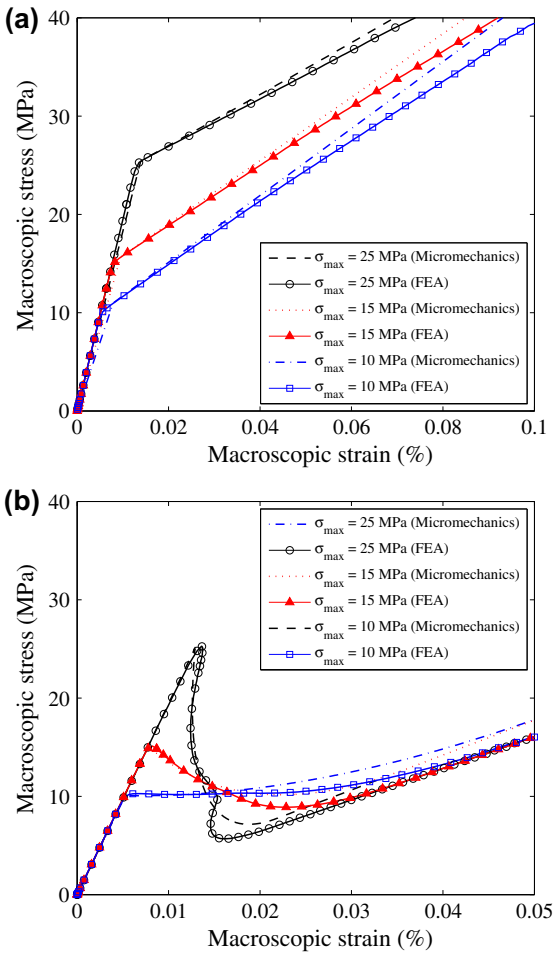

Fig. 18. Effect of the cohesive strength on the constitutive relationship with particle size of: (a) 100 μm and (b) 2 mm.

5.6. Remarks

Both theoretical and computational results agree well each other (see Figs. 15–18), especially when the strain is small. The results from the finite element analysis (FEA) are described by a solid line with markers, and the results from the micromechanics model are illustrated by a dashed, dotted or dashed-dotted line. When the macroscopic strain increases, the finite element results with the cohesive zone model deviate slightly from the micromechanics results. The difference may result from the fact that the finite element formulation considers geometrical nonlinearity with finite strains while the micromechanics model is based on small strain theory.

6. Case study: determination of the PPR cohesive relation

Macroscopic cohesive behavior of composite material might provide some important information to determine the PPR cohesive relation (Eq. (22)) for the particle/matrix interfaces. To illustrate the method that is used to estimate the key parameters in the PPR cohesive relation, we use the macroscopic cohesive behavior of PBX 9501 from Tan et al. [15] as an example. The material PBX 9501 is a high explosive material, which consists of polymeric binder matrix with elastic modulus $E^m = 1$ MPa, Poisson's ratio $\nu^m = 0.499$ and energetic HMX particles with bulk modulus $K^p = 12.5$ GPa. The size distribution of HMX particles can be considered as a bimodal distribution with the large particles having radii $a_1 = 125$ μm, and the small particles having radii $a_2 = 4$ μm, with corresponding volume fractions of $f_1 = 69.5\%$ and $f_2 = 23.2\%$, respectively. The macroscopic cohesive relation of PBX 9501 between the macroscopic stress $\bar{\sigma}$ (normalized by the elastic modulus $\bar{E}$ of PBX 9501, which is 1 GPa [40]) and the opening displacement can be obtained from a mode I fracture test of the modified compact tension specimen, as shown in Fig. 19. In stage 1, the macroscopic cohesive stress $\bar{\sigma}$ increases linearly from zero to the macroscopic cohesive strength $\bar{\sigma}_{\max} = 1.66$ MPa with a very high slope. Stage 2 is the softening stage, where the cohesive stress decreases approximately linearly from $\bar{\sigma}_{\max}$ to zero when the separation reaches the final crack width. If separation

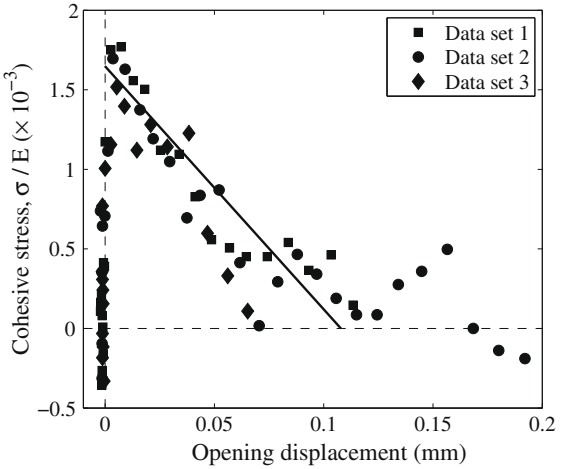

Fig. 19. Case study: macroscopic cohesive relation of the high explosive material PBX 9501 [15].

is greater than the critical crack width (or final crack width) of 0.11 mm, the macroscopic cohesive relation is in stage 3, where the interface is completely debonded, and hence the macroscopic cohesive stress is always zero. The macroscopic cohesive fracture energy, or the total area below the cohesive stress–displacement curve in Fig. 19, is measured as 89 N/m. The initial bulk modulus $\bar{K}$ of PBX 9501 is reported as 1.11 GPa [40].

The important data from the modified compact tension test of PBX 9501, such as the shape of macroscopic cohesive relation, the macroscopic fracture energy, the macroscopic cohesive strength and the initial bulk modulus, can be used to determine the four cohesive parameters: cohesive strength $\sigma_{\max}$, cohesive fracture energy ϕ_n, shape parameter α, and initial slope indicator λ_n in the PPR cohesive relation. It is important to note that the stress state ahead the crack tip in the mode I fracture test of the modified specimen can be approximated as a hydrostatic stress state because of large stress triaxiality [37]. This approximation helps us to apply our micromechanics model in hydrostatic tension loading, as presented in the previous sections, to determine the relation of these microscopic cohesive parameters to the properties of macroscopic behavior of the material, which are presented next.

6.1. Shape of macroscopic cohesive relation

In Fig. 19, the macroscopic cohesive relation of PBX 9501 shows a linear softening stage after the peak stress. We assume that the microscopic cohesive relation also has a similar linear softening shape. Therefore, the shape parameter α could be estimated as 2.

6.2. Macroscopic fracture energy

To obtain the fracture energy of the microscopic cohesive relation, Tan et al. [15] proposed using energy balance along the "path of interface debonding" between the total macroscopic fracture energy release and the total microscopic energy release, which accounts for both microscopic fracture energy release from particle/matrix debonding and energy release due to tearing of the matrix. They estimated the fracture energy ϕ_n of particle/matrix interface in PBX 9501 as $\phi_n = 81$ N/m.

6.3. Initial bulk modulus

At the initial stage of loading the specimen, the normal displacement separation, Δ_n, of the particle/matrix interface is very small, hence the cohesive relation in Eq. (22) can be linearized in terms of Δ_n as

$$\sigma^{\text{int}} = k^{\text{int}}\Delta_n, \quad k^{\text{int}} = \frac{\phi_n}{\delta_n^2}\left(\frac{\alpha}{m}\right)^m\left(\frac{m}{\alpha}\right)^{m-1}(m+\alpha), \tag{25}$$

where k^{int} is a function of $\sigma_{\max}$ and λ_n.

For the case of a linear relation between microscopic cohesive stress and the normal displacement separation under the hydrostatic tension loading, using the Mori–Tanaka method, Tan et al. [36] derived a formula to determine initial bulk modulus $\bar{K}$ for a composite with two different particle sizes that is given as

$$\overline{K} = \frac{1}{3}\frac{d\bar{\sigma}}{d\bar{\varepsilon}} = \left[\frac{1}{K^m} + \frac{9(1-\nu^m)}{2E^m}\frac{f-\sum_{k=1}^{2} f_k\alpha_k}{1-f+\sum_{k=1}^{2} f_k\alpha_k}\right]^{-1}, \quad \alpha_k = \frac{3(1-\nu^m)}{2E^m\left(\frac{1}{k^{\text{int}}a_k} + \frac{1+\nu^m}{2E^m} + \frac{1}{3K^p}\right)}, \tag{26}$$

Table 2
Properties of high explosive material PBX9501.

Definition	Symbol	Value
PPR shape parameter	α	2
PPR cohesive fracture energy	ϕ_n	81 N/m
PPR initial slope indicator	λ_n	0.006
PPR cohesive strength	$\sigma_{\max}$	1.6672 MPa
Initial effective bulk modulus	$\bar{K}$	1.11 GPa
Polymeric binder matrix elastic modulus	E^m	1 MPa
Polymeric binder matrix Poisson's ratio	ν^m	0.499
HMX particle bulk modulus	K^p	12.5 GPa
Large particle radius	a_1	125 μm
Small particle radius	a_2	4 μm
Large particle volume fraction	f_1	69.5%
Small particle volume fraction	f_2	23.2%
Macroscopic cohesive strength	$\bar{\sigma}_{\max}$	1.66 MPa
Microscopic cohesive stress of the large particle	σ_1^{int}	1.6672 MPa ($\approx\sigma_{\max}$)
Microscopic cohesive stress of the small particle	σ_2^{int}	1.6355 MPa

where K^m and K^p are the elastic bulk moduli of the matrix and particle, respectively. With the value of initial bulk modulus $\bar{K} = 1.11$ GPa, Eq. (26) provides a nonlinear equation in terms of $\sigma_{\max}$ and λ_n.

6.4. Macroscopic cohesive strength

Rae et al. [41] observed that debonding between particle and matrix appears first for the large particles in PBX 9501. Therefore, when the macroscopic cohesive stress $\bar{\sigma}$ reaches its peak (macroscopic cohesive strength), the microscopic cohesive stress of the large particle σ_1^{int} reaches the cohesive strength $\sigma_{\max}$, while the microscopic cohesive stress of the small particle reaches $\sigma_2^{\text{int}} (< \sigma_{\max})$.

The relation between the macroscopic cohesive stress and the microscopic cohesive stresses for composite material with two particle sizes is given as

$$\bar{\sigma} = (1-f)\bar{\sigma}^m + f_1\sigma_1^{\text{int}} + f_2\sigma_2^{\text{int}}. \tag{27}$$

The normal displacement separations for each particle size can be obtained by the Mori–Tanaka method as

$$(\Delta_n)_k = a_k\left[\frac{3(1-\nu^m)}{2E^m}\sigma^m - \left(\frac{1+\nu^m}{2E^m} + \frac{1-2\nu^p}{E^p}\right)\sigma_k^{\text{int}}\right], \quad k = 1,2. \tag{28}$$

Cohesive relations for each particle size are given as

$$\sigma_k^{\text{int}} = \frac{\phi_n}{\delta_n}\left(\frac{\alpha}{m}\right)^m\left(1-\frac{(\Delta_n)_k}{\delta_n}\right)^{\alpha-1}\left(\frac{m}{\alpha}+\frac{(\Delta_n)_k}{\delta_n}\right)^{m-1}(m+\alpha)\frac{(\Delta_n)_k}{\delta_n}, \quad k = 1,2. \tag{29}$$

By substituting Eqs. (27) and (28) into Eq. (29), when $\bar{\sigma}$ reaches $\bar{\sigma}_{\max} = 1.66$ MPa, we obtain two nonlinear equations in terms of $\sigma_{\max}, \sigma_2^{\text{int}}$, and λ_n as

$$\sigma_{\max} = h(\sigma_{\max}, \sigma_2^{\text{int}}, \lambda_n), \tag{30}$$

$$\sigma_2^{\text{int}} = g(\sigma_{\max}, \sigma_2^{\text{int}}, \lambda_n). \tag{31}$$

The cohesive strength $\sigma_{\max}$ and the initial slope indicator λ_n of the PPR cohesive relation can be determined simultaneously from the initial bulk modulus of PBX 9501 and the macroscopic cohesive strength. Thus Eqs. (30) and (31), together with Eq. (26) when $\bar{K} = 1.11$ GPa, provide a system of three nonlinear equations with three unknowns $\sigma_{\max}, \sigma_2^{\text{int}}$, and λ_n. This system can be solved by using a nonlinear equations solver and the solutions for $\sigma_{\max}, \sigma_2^{\text{int}}$, and λ_n are obtained as 1.6672 MPa, 1.6355 MPa and 0.006, respectively. The results are summarized in Table 2.

7. Concluding remarks

Effective macroscopic behavior is investigated by means of an integrated approach involving micromechanics and a computational model. For the micromechanics investigation, the extended Mori–Tanaka model is incorporated with the PPR potential-based cohesive zone model. The computational analysis is performed by utilizing the finite element-based cohesive zone model in two-dimensions (plane strain). The effects of the PPR cohesive parameters, particle size and volume fraction on the constitutive relationship of material with microstructures are investigated for hydrostatic tensile stress state and

equi-biaxial tension state. In general, the overall behavior observed considering hydrostatic tensile stress state (Figs. 3–8) is qualitatively similar to the behavior observed considering equi-biaxial tension state (Figs. 15–18). In addition, the microstructural debonding process is uniform when the macroscopic stress–strain relationship demonstrates hardening or softening behavior (cf. Figs. 12a and 13). On the other hand, non-uniform microstructural debonding process is observed when the macroscopic stress–strain relationship demonstrates snap-back instability (cf. Figs. 12b and 14). The results of the micromechanics model demonstrate agreement with the results from the computational model. Finally, through multiscale arguments, the cohesive parameters of the PPR model are estimated using macroscopic cohesive behavior of composite material in conjunction with micromechanics theory.

Acknowledgements

The authors acknowledge support from the National Science Foundation (NSF) through Grant #0800805. Duc Ngo also acknowledges support from Vietnam Education Foundation (VEF). The information presented in this paper is the sole opinion of the authors and does not necessarily reflect the views of the sponsoring agencies. Finally, the authors thank the anonymous reviewers for constructive and thorough revision of the work.

References

[1] Mura T. Micromechanics of defects in solids Norwell. MA: Kluwer Academic Publishers; 1987.
[2] Nemat-Nasser S, Hori M. Micromechanics: overall properties of heterogeneous materials. Amsterdam (The Netherlands): North Holland; 1999.
[3] Budiansky B. On the elastic moduli of some heterogeneous materials. J Mech Phys Solids 1965;13(4):223–7.
[4] Hill R. A self-consistent mechanics of composite materials. J Mech Phys Solids 1965;13(4):213–22.
[5] Christensen RM, Lo KH. Solutions for effective shear properties in three phase sphere and cylinder models. J Mech Phys Solids 1979;27(4):315–30.
[6] Mori T, Tanaka K. Average stress in matrix and average elastic energy of materials with misfitting inclusions. Acta Metall 1973;21(5):571–4.
[7] Tan H, Huang Y, Liu C, Ravichandran G, Paulino GH. Constitutive behaviors of composites with interface debonding: the extended Mori–Tanaka method for uniaxial tension. Int J Fract 2007;146(3):139–48.
[8] Yin HM, Sun LZ, Paulino GH. Micromechanics-based elastic model for functionally graded materials with particle interactions. Acta Mater 2004;52(12):3535–43.
[9] Yin HM, Paulino GH, Buttlar WG, Sun LZ. Micromechanics-based thermoelastic model for functionally graded particulate materials with particle interactions. J Mech Phys Solids 2007;55(1):132–60.
[10] Paulino GH, Yin HM, Sun LZ. Micromechanics-based interfacial debonding model for damage of functionally graded materials with particle interactions. Int J Damage Mech 2006;15(3):267–88.
[11] Levy AJ. Separation at a circular interface under biaxial load. J Mech Phys Solids 1994;42(7):1087–104.
[12] Siegmund T, Brocks W. Prediction of the work separation and implications to modeling. Int J Fract 1999;99(1–2):97–116.
[13] Needleman A, Tvergaard V. Analysis of ductile rupture in notched bars. J Mech Phys Solids 1984;32(6):461–90.
[14] Allen DH, Searcy CR. Micromechanical model for a viscoelastic cohesive zone. Int J Fract 2001;107(2):159–76.
[15] Tan H, Liu C, Huang Y, Geubelle PH. The cohesive law for the particle/matrix interfaces in high explosives. J Mech Phys Solids 2005;53(8):1892–917.
[16] Shen YL, Finot M, Needleman A, Suresh S. Effective elastic response of two-phase composites. Acta Metall Mater 1994;42(1):77–97.
[17] Shen YL, Finot M, Needleman A, Suresh S. Effective plastic response of two-phase composites. Acta Metall Mater 1995;43(4):1701–22.
[18] Xu XP, Needleman A. Void nucleation by inclusion debonding in a crystal matrix. Modell Simul Mater Sci Engng 1993;1(2):111–32.
[19] Finot M, Shen YL, Needleman A, Suresh S. Micromechanical modeling of reinforcement fracture in particle-reinforced metal-matrix composites. Metall Mater Trans A 1994;25 A(11):2403–20.
[20] Mogilevskaya SG, Crouch SL. A Galerkin boundary integral method for multiple circular elastic inclusions with homogeneously imperfect interfaces. Int J Solids Struct 2002;39(18):4723–46.
[21] Carpinteri A, Paggi M, Zavarise G. Snap-back instability in micro-structured composites and its connection with superplasticity. Strength Fract Complexity 2005;3(2–4):61–72.
[22] Dugdale DS. Yielding of steel sheets containing slits. J Mech Phys Solids 1960;8(2):100–4.
[23] Barenblatt GI. Mathematical theory of equilibrium cracks in brittle fracture. Adv Appl Mech 1962;7:55–129.
[24] Boone TJ, Wawrzynek PA, Ingraffea AR. Simulation of the fracture process in rock with application to hydrofracturing. Int J Rock Mech Min Sci 1986;23(3):255–65.
[25] Ingraffea AR, Gerstle WH, Gergely P, Saouma V. Fracture mechanics of bond in reinforced concrete. J Struct Engng 1984;110(4):871–90.
[26] Xu XP, Needleman A. Numerical simulations of fast crack growth in brittle solids. J Mech Phys Solids 1994;42(9):1397–434.
[27] Han T-S, Ural A, Chen C-S, Zehnder AT, Ingraffea AR, Billington SL. Delamination buckling and propagation analysis of honeycomb panels using a cohesive element approach. Int J Fract 2002;115(2):101–23.
[28] Song SH, Paulino GH, Buttlar WG. A bilinear cohesive zone model tailored for fracture of asphalt concrete considering viscoelastic bulk material. Engng Fract Mech 2006;73(18):2829–48.
[29] Zhang ZJ, Paulino GH, Celes W. Extrinsic cohesive modelling of dynamic fracture and microbranching instability in brittle materials. Int J Numer Methods Engng 2007;72(8):893–923.
[30] Tvergaard V, Hutchinson JW. Influence of plasticity on mixed mode interface toughness. J Mech Phys Solids 1993;41(6):1119–35.
[31] Park K, Paulino GH, Roesler JR. A unified potential-based cohesive model of mixed-mode fracture. J Mech Phys Solids 2009;57(6):891–908.
[32] Taya M, Chou T-W. On two kinds of ellipsoidal inhomogeneities in an infinite elastic body: an application to a hybrid composite. Int J Solids Struct 1981;17(6):553–63.
[33] Weng GJ. Some elastic properties of reinforced solids with special reference to isotropic ones containing spherical inclusions. Int J Engng Sci 1984;22(7):845–56.
[34] Weng GJ. The overall elastoplastic stress–strain relations of dual-phase metals. J Mech Phys Solids 1990;38(3):419–41.
[35] Benveniste Y. A new approach to the application of Mori–Tanaka's theory in composite materials. Mech Mater 1987;6(2):147–57.
[36] Tan H, Huang Y, Liu C, Geubelle PH. The Mori–Tanaka method for composite materials with nonlinear interface debonding. Int J Plast 2005;21(10):1890–918.
[37] McMeeking RM, Parks DM. On criteria for J-dominance of crack-tip fields in large-scale yielding elastic–plastic fracture. Atlanta (GA): ASTM Special Technical Publication; 1979. p. 175–94.
[38] Bazant ZP, Planas J. Fracture and size effect in concrete and other quasibrittle materials. Boca Raton: CRC Press; 1998.
[39] Hillerborg A, Modéer M, Petersson PE. Analysis of crack formation and crack growth in concrete by means of fracture mechanics and finite elements. Cem Concr Res 1976;6(6):773–81.

[40] Gray GT, III, Idar DJ, Blumenthal WR, Cady CM, Peterson PD. High- and low-strain rate compression properties of several energetic material composites as a function of strain rate and temperature. In: Proceedings of the 11th international detonation symposium. Snowmass (CO); 1998. p. 76–87.
[41] Rae PJ, Palmer SJP, Goldrein HT, Field JE, Lewis AL. Quasi-static studies of the deformation and failure of PBX 9501. Proc Royal Soc Lond Ser A (Math Phys Engng Sci) 2002;458(2025):2227–42.